







Three-Dimensional Polarimetric InSAR Imaging of Non-Cooperative Targets

Ajeet Kumar , *Member, IEEE*, Elisa Giusti , *Member, IEEE*,
 Francesco Mancuso , *Graduate Student Member, IEEE*, Selenia Ghio , *Member, IEEE*,
 Alberto Lupidi , *Member, IEEE*, and Marco Martorella , *Fellow, IEEE*

Abstract—A new Polarimetric Interferometry Inverse Synthetic Aperture Radar (Pol-InSAR) 3D imaging method for non-cooperative targets is proposed in this paper. 3D imaging of non-cooperative targets becomes possible by combining additional information of interferometric phase along with conventional 2D ISAR imaging. In the previously reported single-polarimetry InSAR based 3D imaging, only a single-channel based interferometric phase is available that can be exploited to reconstruct the 3D ISAR image. This limits the ability to obtain a full target's scattering response and therefore limits the estimation of an accurate interferometric phase. To overcome this constraint, full-polarimetry information is being exploited in this paper, which allows to select the optimal polarimetric combination through which the highest coherence can be obtained. A higher coherence leads to a reduction (optimally a minimization) of the phase estimation error. Consequently, with an optimal phase estimation, an accurate 3D imaging of the target is possible. To validate this proposed Pol-InSAR based 3D imaging approach, both simulated and real datasets are taken under consideration.

Index Terms—ISAR, pol-InSAR, polarimetry, interferometry, In-SAR, 3D imaging, non-cooperative target, Tank-72.

I. INTRODUCTION

SYNTHETIC Aperture Radar (SAR) and Inverse SAR (ISAR) systems are well known to obtain high-resolution images by exploiting the relative motion between radar-platform and target. The SAR systems are usually mounted on the spaceborne or airborne radar-platforms moving with the known motion $v(f, t)$. Considering stationary target under observation, SAR systems exploit $v(f, t)$ information to coherently process the received echoes. But lamentably, these type of systems are sensitive to the uncertainties in the target motion that results in blurred and misplaced images for non-cooperative moving targets [1]. In contrast, ISAR processing is non-reliant to the

prior knowledge of the relative motion between target and radar platform, that makes ISAR systems most suitable for non-cooperative targets imaging.

The conventional way of imaging non-cooperative target using ISAR is by forming two-dimensional (2D) electromagnetic images [2], [3], [4]. The 2D ISAR images do not map the target in its actual form, rather, these images are only filtered projection of actual 3D targets' reflectivity onto an image projection plane (IPP). Moreover, the IPP orientation is not priori known as it firmly depends on the unknown parameters of the target, such as target-movement and target-geometry [5]. To overcome the demerits of 2D ISAR imaging system, 3D imaging is attempted in the literature that tries to detect the target in its true 3D form [6], [7], [8], [9], [10], [11], [12], [13]. The most promising and reliable attempt reported so far is Interferometry ISAR (InSAR) based approach that performs 3D imaging in the form of point cloud indicating the actual shape of the target [14]. This 3D InSAR algorithm is in fact validated through real implementation of ground-based as well as airborne-platform-based Interferometric ISAR systems [14], [15], [16], [17]. In 3D InSAR approaches, the 3D image of the target is generated by combining the interferometry phase along with the traditional 2D ISAR imaging.

Almost all the reported 3D InSAR approaches utilize single-polarimetry (single-pol) information. Single-pol systems transmit on one polarization and receive the same (like) polarization that produces limited information about the target. This single-channel backscattering information is not sufficient to identify the wide variety of scattering responses coming from the scatterers constituting complex target structures, such as ships, tanks, aircraft, etc. As a result, these conventional systems can miss to identify reliable or strong scatterers generating responses in polarimetric channels other than the one acquired by the corresponding single-pol system [2]. Furthermore, the single-pol 3D InSAR system allows to calculate single-channel based interferogram information only. These conventional systems are forced to use the available single polarimetric channel for height estimation, although it could happen that the estimated interferometric phase is not the optimal one. To overcome these limitations of single-pol 3D InSAR systems, a new Polarimetric Interferometry Inverse Synthetic Aperture Radar (Pol-InSAR) 3D imaging approach is established in this paper that takes full-polarimetry (full-pol) back-scattered information into account. This proposed method is the first attempt to establish a complete

Manuscript received 11 September 2022; revised 24 December 2022; accepted 8 February 2023. Date of publication 24 February 2023; date of current version 8 March 2023. This work was supported by the Office of Naval Research Global (ONR Global) under Grant N62909-20-1-2062, entitled ATR by means of Polarimetric ISAR Images and multi-view 3D InSAR. The associate editor coordinating the review of this manuscript and approving it for publication was Dr. Ilaria Catapano. (*Corresponding author: Ajeet Kumar.*)

Ajeet Kumar, Elisa Giusti, Francesco Mancuso, Selenia Ghio, and Alberto Lupidi are with the Radar and Surveillance Systems (RaSS) National Laboratory of CNIT, 56124 Pisa, Italy (e-mail: ajeet.kumar.in@ieee.org; elisa.giusti@cnit.it; francesco.mancuso@cnit.it; selenia.ghio@cnit.it; alberto.lupidi@cnit.it).

Marco Martorella is with the Department of Information Engineering, University of Pisa, 56122 Pisa, Italy (e-mail: marco.martorella@iet.unipi.it).

Digital Object Identifier 10.1109/TCI.2023.3248942

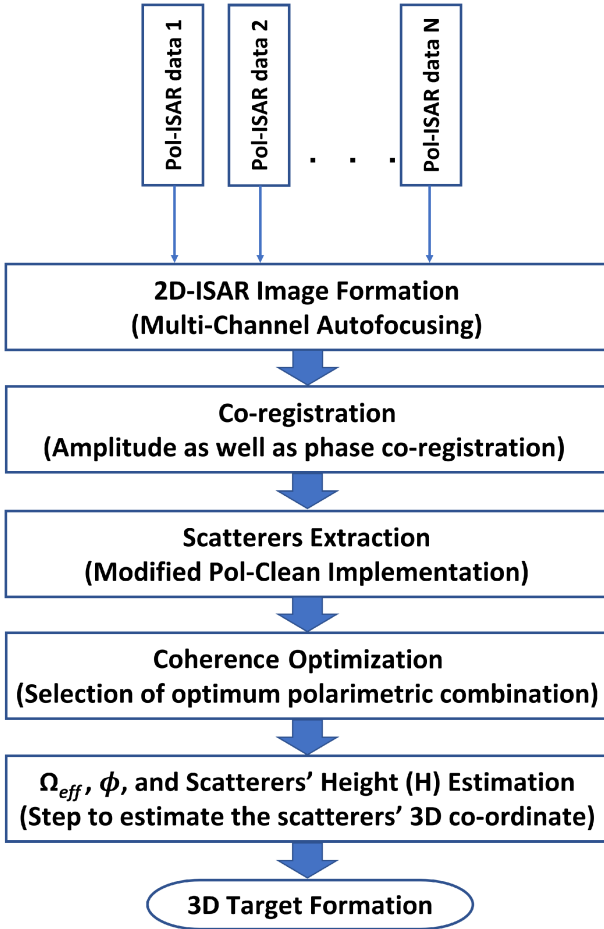


Fig. 1. General block diagram explaining the steps involved in 3D imaging of the target using Pol-InISAR based proposed approach.

procedure of polarimetric interferometry based 3D imaging of non-cooperative targets that utilizes the most reliable scatterers to form 3D images with their optimized phase information. Consequently, high coherence levels and correct 3D imaging results are being achieved. The proposed Pol-InISAR approach also significantly reduces the computational burden by discarding the un-reliable scatterers. As a result, this method can become a vital asset for establishing a real time ATR (Automatic Target Recognition) system for non-cooperative targets. The utilization of full-polarimetry information in this presented 3D imaging approach facilitates to obtain the interferogram phase from all possible linear combinations of the polarization states. Further among these combinations, the optimum one, generating the highest possible coherence level, can be selected. As one of the vital steps of the proposed Pol-InISAR method, this coherence optimization technique is implemented here for the first time for ISAR application of non-cooperative target detection.

The complete description of the proposed Pol-InISAR method is presented in Section II. The whole process of 3D image generation involves five vital steps as depicted in Fig. 1. These steps are explained in details in Section II. The proposed Pol-InISAR method has been validated using both simulated and real ISAR datasets. A detailed description of both datasets is added in

Section III. Further, the results and corresponding analysis are added in Section IV. Final conclusion is drawn in Section V.

II. POL-INISAR BASED 3D IMAGING OF TARGET: A PROPOSED APPROACH

The proposed Pol-InISAR method involves five significant steps to form 3D image of the target. These steps are depicted in the block diagram shown in Fig. 1. Among the five steps of the proposed approach, the coherence optimization and scatterers extraction involve full-polarimetry information and require to be implemented together to get optimized 3D results. These steps are described below in detail followed by the other steps involved in the proposed Pol-InISAR based 3D imaging method.

The single-polarimetry based conventional 3D InISAR system acquires propagation delay phase (ϕ_p) that allows to calculate single-channel based interferogram information only. Conversely, the full-polarimetry based 3D InISAR system acquires scattering information phase (ϕ_s) and the propagation delay phase. By combining the ϕ_p and ϕ_s phase values along with the other information associated with full-polarimetry, the interferogram from all possible linear combinations of polarization states can be obtained. Further among these combinations, the optimum one associated with maximum possible coherence, can be selected. The polarimetric combination achieving the highest possible coherence reduces any chance of uncertainties in the interferogram phase [18], and therefore can generate the most reliable height estimation leading to the optimum 3D target reconstruction.

The coherence optimization based selection of optimum polarimetric combination has previously been investigated for natural scatterers [19], [20]. In general, these types of scatterers exhibit common polarimetric features. Contrarily, in the case of man-made complex non-cooperative targets, each scatterer can exhibit proper polarimetric behavior and therefore the corresponding processing should be applied to each scatterer individually that composes the target. In this paper, the full-polarimetry ISAR based coherence optimization approach is being first time investigated for Inverse SAR applications of complex non-cooperative target detection. The two datasets implemented for the validation are real Tank-72 (T72) ISAR data and Astice boat simulator ISAR data, both exhibiting complex target structure scenarios. The Tank-72 and boat simulator datasets exhibit two-acquisitions or single-baseline and three-acquisitions or dual-baseline based InISAR scenarios, respectively. The coherence optimization based algorithm differs for these two different conditions. For two-acquisitions condition, the single-baseline coherence optimization approach is useful, while for the more than two-acquisitions condition, multiple-baseline coherence optimization can be used. Both of these methods are described below in detail.

A. Two-Acquisitions Based Coherence Optimization Approach

The full-polarimetry ISAR data acquired by the two antennas situated at two different points in space can be expressed in terms

of the scattering vectors k_1 and k_2 , as follows.

$$k_1 = [S_{HH}^1 + S_{VV}^1 \ S_{HH}^1 - S_{VV}^1 \ 2S_{HV}^1]^T \quad (1)$$

$$k_2 = [S_{HH}^2 + S_{VV}^2 \ S_{HH}^2 - S_{VV}^2 \ 2S_{HV}^2]^T \quad (2)$$

Further, by performing the outer product formed from k_1 and k_2 , the 6×6 polarimetric interferometry matrix ($[T_6]$) can be generated as

$$[T_6] = \left\langle \begin{bmatrix} k_1 \\ k_2 \end{bmatrix} \cdot \begin{bmatrix} k_1^\dagger & k_2^\dagger \end{bmatrix} \right\rangle = \begin{bmatrix} T_{11} & \Omega_{12} \\ \Omega_{12}^\dagger & T_{22} \end{bmatrix}, \quad (3)$$

where \dagger and $\langle \cdot \rangle$ indicate Hermitian matrix transpose and ensemble averaging, respectively. The matrices T_{11} and T_{22} contain polarimetric information, whereas the matrix Ω_{12} contains polarimetric as well as interferometry information. By jointly utilizing these matrices, the projection vector/vectors can be derived that helps to project k_1 and k_2 into two new polarimetric combinations which maximize the coherence between two acquisitions. The most general approach based on two projection vectors (w_1 and w_2) was established by Cloude et al. in [19]. Being these vectors complex, the use of two different projection vectors (w_1 and w_2) for the two channels, can induce an undesired phase shift in the interferogram, if $\arg(w_1^\dagger w_2) \neq 0$ [20], [21]. This erroneous phase shift can be avoided by using a single or unique projection vector (w) based new approach, established by modifying the conventional optimization theory [22], [23]. In this new approach, the scattering coefficients for two different acquisitions can be estimated by projecting the feature scattering vectors (k_1 and k_2) as $\mu_1 = w^\dagger k_1$ and $\mu_2 = w^\dagger k_2$. Consequently, the coherence (γ_w) and phase ($\arg(\gamma_w)$) can be calculated as

$$\gamma_w = \frac{\langle \mu_1 \mu_2^* \rangle}{\sqrt{\langle \mu_1 \mu_1^* \rangle \langle \mu_2 \mu_2^* \rangle}} = \frac{w^\dagger [\Omega_{12}] w}{\sqrt{(w^\dagger [T_{11}] w)(w^\dagger [T_{22}] w)}} \quad (4)$$

$$\arg(\gamma_w) = \arg(\langle \mu_1 \mu_2^* \rangle) = \arg(w^\dagger [\Omega_{12}] w). \quad (5)$$

Further, the value of the unique projection vector leading to the highest possible coherence value is obtained based on the following optimization function

$$\tilde{w} = \arg \max_w |\gamma_w| \quad (6)$$

This optimization criterion can be met, and \tilde{w} can be evaluated by setting gradient of $|\gamma_w|^2$ to zero and solving it with the help of (4). A detailed derivation of this approach is added in Appendix. As derived in Appendix, the solution of coherence optimization converges to the following 3×3 eigenvalue problem through which the requisite w can be obtained.

$$Hw = \lambda w \quad (7)$$

where H is a Hermitian matrix [22] that can be represented as

$$H = (T_{11} + T_{22})^{-1} (\Omega_{12} + \Omega_{12}^\dagger) \quad (8)$$

It is worth noting from (27) of Appendix that the parameter λ in (7) is nothing but the amplitude of coherence value. Equation (7) provides three eigenvectors among which the one corresponding to the highest eigenvalue λ_{\max} (indicating maximum coherence condition) needs to be selected as a unique projection vector \tilde{w} .

Further, by putting $w = \tilde{w}$ in (4) and (5), the optimized coherence ($\tilde{\gamma}_w$) and the optimized phase ($\arg(\tilde{\gamma}_w)$) can be obtained, respectively. The coherence $\tilde{\gamma}_w$ is the optimized coherence value attaining highest possible value and the corresponding phase $\arg(\tilde{\gamma}_w)$ is the optimized phase leading to a better and reliable 3D reconstruction.

This aforementioned approach is suitable for the scenario when full-polarimetry data acquired in two acquisitions from two different points in space, generating Pol-InISAR information, such as for the case of T72 data implemented in this paper. However, for the condition of more than two acquisitions, an extended version of this method, i.e. multiple-acquisitions based optimization approach [24] is described below in details.

B. Multiple-Acquisitions Based Coherence Optimization Approach

In more than two acquisitions from different points in space, such as for the case of boat simulator data implemented in this paper, the acquired full-polarimetry information can be expressed in terms of scattering vector as,

$$k_i = [S_{HH}^i + S_{VV}^i \ S_{HH}^i - S_{VV}^i \ 2S_{HV}^i]^T \quad (9)$$

where $i \in (1, 2, \dots, N)$ for N number of antennas. In this paper, we implemented multiple-acquisitions based coherence optimization approach only for three-acquisitions condition, so hereafter $N = 3$ is considered. For this condition, the combined polarimetric interferometry matrix can be written as follows.

$$[T_9] = \left\langle \begin{bmatrix} k_1 \\ k_2 \\ k_3 \end{bmatrix} \cdot \begin{bmatrix} k_1^\dagger & k_2^\dagger & k_3^\dagger \end{bmatrix} \right\rangle = \begin{bmatrix} T_{11} & \Omega_{12} & \Omega_{13} \\ \Omega_{12}^\dagger & T_{22} & \Omega_{23} \\ \Omega_{13}^\dagger & \Omega_{23}^\dagger & T_{33} \end{bmatrix} \quad (10)$$

The matrices T_{11} , T_{22} , and T_{33} contain polarimetric information associated with the three different antennas, whereas Ω_{12} , Ω_{13} , and Ω_{23} contain polarimetry as well as interferometry information associated with antennas: first - second, first - third, and second - third, respectively. Similar to the two-acquisitions based optimization approach, in this three-acquisitions condition, the sum of coherence parameters, i.e. $\sum |\gamma_{ij}|$ is taken as the optimization criterion to evaluate the unique projection vector (\tilde{w}) based on the following optimization function

$$\tilde{w} = \arg \max_w \sum_{i=1}^3 \sum_{j=1, j \neq i}^3 |\gamma_{ij}| \quad (11)$$

where γ_{ij} can be expressed as

$$\gamma_{ij} = w^\dagger \Pi_{ij} w \quad (12)$$

In (12), the parameters Π_{ij} and w can be estimated as

$$w = \frac{\sqrt{T_e} w}{w^\dagger \sqrt{T_e} w}; \Pi_{ij} = T_e^{-1/2} \Omega_{ij} T_e^{-1/2}; T_e = \frac{1}{3} \sum_1^3 T_{ii} \quad (13)$$

We adopted here the Multi-Baseline ESM (MB-ESM) optimization approach of [24] to estimate the unique projection vector (\tilde{w}). The simplified version of the corresponding method for our three-acquisitions condition is summarized in the iterative based

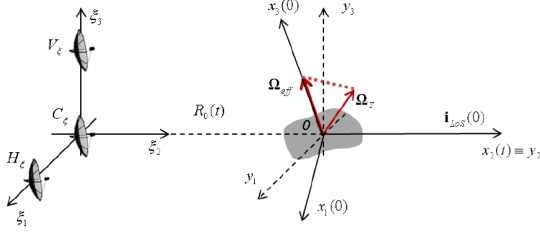


Fig. 2. Radar target geometry of boat simulator full-polarimetry (full-pol) ISAR data.

TABLE I
RADAR PARAMETERS OF BOAT SIMULATOR

Parameters	Value
Polarization	HH, HV, VH, VV
Career Frequency	10 GHz
Frequency Range	9.85 GHz - 10.15 GHz
Frequency Step	1.17 MHz
Frequency Bandwidth	300 MHz
No. of Transmitted Frequency	256
No. of Sweeps	128
Target Velocity	20 m/s
[Roll, Pitch, Yaw]	[10°, 20°, 60°]
[Horizontal & Vertical Baseline]	[1m, 1m]

approach described in Algorithm 1. Further with the estimated \tilde{w} , the full-polarimetry information of the three antennas V_ξ , C_ξ , and H_ξ can be projected to estimate the corresponding scattering coefficients as $\mu_1 = \tilde{w}^\dagger k_1$, $\mu_2 = \tilde{w}^\dagger k_2$, and $\mu_3 = \tilde{w}^\dagger k_3$. These three scattering coefficients can generate optimum $\sum |\tilde{\gamma}_{ij}|$ as well as optimum interferometric phases leading to better and reliable 3D reconstruction.

However, before implementing the coherence optimization approach in the proposed Pol-InISAR 3D imaging method, the scattering center extraction through the polarimetry CLEAN (Pol-CLEAN) is required. This Pol-CLEAN process not only reduces the computational burden significantly but also gives rise the reliable scatterers that can be taken as input in the aforementioned coherence optimization process. The coherent optimization approach needs to be applied individually only on these extracted scatterers, which are reliable and can generate the highest possible coherence values. In this proposed work, the modified version of Polarimetry CLEAN (Pol-CLEAN) [25] is used, which extracts scatterers better than the classical Pol-CLEAN [26] by additionally suppressing the interference coming from nearby scatterers.

With the help of the two aforementioned full-polarimetry information based steps: coherent optimization and modified Pol-CLEAN, the reconstructed 3D point cloud can be formed through the procedure indicated in Fig. 1. The block diagram shown in this figure indicates steps for general Pol-InISAR based 3D target formation, where N , $\forall N > 1$ number of Pol-ISAR datasets acquired from N different points in space, are utilized to form the 3D point cloud. In this paper, we outlined the procedure for two specific cases of $N = 2$ and $N = 3$ corresponding to the T72 and boat simulator datasets, respectively. However,

Algorithm 1: An Algorithm for Three-Acquisitions Based Coherence Optimization.

Procedure

Step-1

Initialize the eigenvalue as $\lambda_{\max} = 0$ and calculate the optimal phase shift as $\theta_{ij} = \arg(\text{trace} \Pi_{ij})$

Step-2

Calculate the Hermitian Matrix (H) as

$$H = \sum_{i=1}^3 \sum_{j=1, j \neq i}^3 \Pi_{ij} e^{-i\theta_{ij}}.$$

Consequently, the eigenvalues and eigenvectors can be obtained from $Hw = \lambda w$.

Step-3

loop:

Update maximum eigenvalue $\lambda_{\max} = \lambda_{\max}^u$, and eigenvector (w) by selecting the largest obtained eigenvalue, and corresponding eigenvector, respectively.

Step-4

Further with the updated information, it is needed to estimate the optimal phase $\theta_{ij}^u = \arg(w^\dagger \Pi_{ij} w)$ and again with θ_{ij}^u , calculate the updated H^u from:

$$H^u = \sum_{i=1}^3 \sum_{j=1, j \neq i}^3 \Pi_{ij} e^{-i\theta_{ij}^u}.$$

By solving $H^u w = \lambda w$, the parameters λ_{\max}^u and w can be further updated by selecting maximum eigenvalue and corresponding eigenvector.

Step-5

if $\lambda_{\max}^u - \lambda_{\max} < \text{eps}$

goto Step-6.

else

goto *loop*.

close;

Here eps indicates the smallest positive number that does not underflow to zero.

Step-6

Finally, the unique projection vector can be calculated by

$$\tilde{w} = \frac{T_e^{-\frac{1}{2}} w}{w^\dagger T_e^{-\frac{1}{2}} w}.$$

further extension of the proposed work can be carried out in the future for multi-baseline configuration by utilizing N ($\forall N > 3$) number of independent observations together to get a more accurate 3D results.

The co-registration step (as mentioned in Fig. 1) is essential to mitigate the effect of images mismatching at each antenna, due to the target motion characteristics and wave path information collected at the different points of acquisitions in space [27]. The complete details of the image co-registration and its utility in 3D target formation can be found in [27], [28], [29]. The following steps are implemented to perform the co-registration [28].

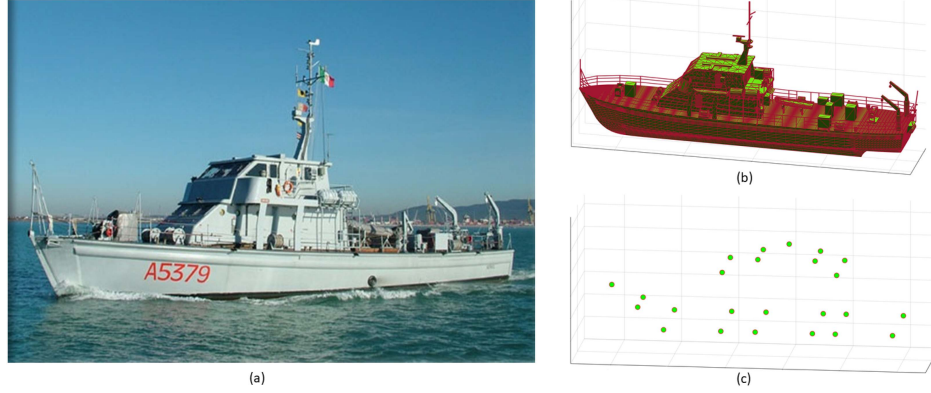


Fig. 3. Image of the target under observation: (a) Actual image of the target (Astice boat) (b) CAD-model corresponding to the target (c) The simulated 3D point scatterer model corresponding to the target.

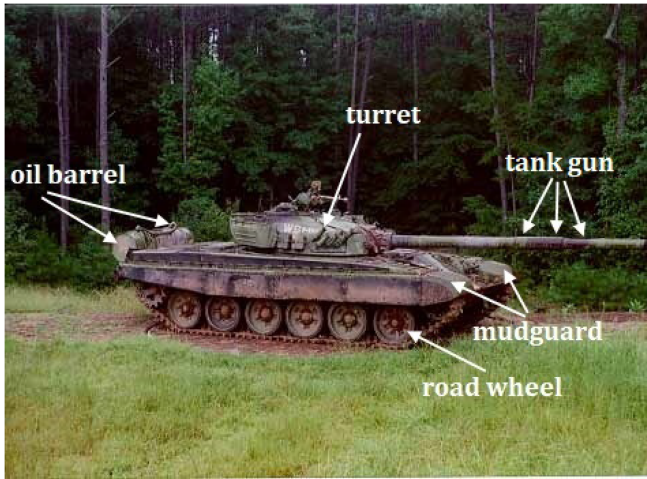


Fig. 4. Image of the target Tank-72 (T72) under observation.

- Select one reliable scatterer, possibly with the highest intensity (brightest scatterer).
- All the images, collected from different points in space are required to be translated or shifted in such a way that the selected scatterer becomes new center of the images at zero Doppler and range coordinates.
- The phase term of the selected scatterer is estimated and further subtracted from the entire images.

The last vital step in Pol-InISAR 3D imaging method is the height estimation (see Fig. 1), which is separately described below for two-acquisitions and three-acquisitions conditions.

After estimating the interferometry phase in two-acquisitions condition, between scattering coefficients μ_1 and μ_2 as described in Section II-A, the height (H_{2A}) of scatterers can be calculated by using the following equation.

$$H_{2A} = \frac{cR_0\Delta\theta_{12}}{4\pi f_0 d_v} \quad (14)$$

where $\Delta\theta_{12}$ is the interferometry phase between the acquired data of two antennas: antenna 1 & antenna 2, as shown in Fig. 5. In the L-type antenna arrangement based three-acquisitions

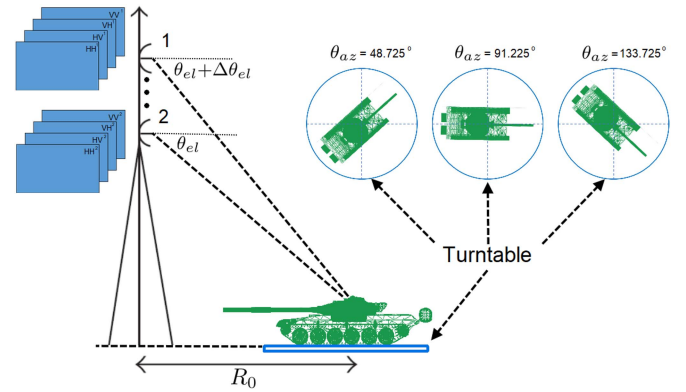


Fig. 5. Radar target geometry of Tank-72 (T72) full-polarimetry (full-pol) ISAR data acquisition. The three azimuth angles (θ_{az}), 48.725° , 91.225° , and 133.725° based acquisition scenarios are also indicated in the image.

TABLE II
RADAR PARAMETERS OF TANK-72 GTRI DATASET

Parameter	Value
Polarization	HH, HV, VH, VV
Central Frequency	9.6 GHz
Frequency Range	9.27 GHz - 9.93 GHz
Frequency Step	3 MHz
No. of Transmitted Frequency	221
No. of Sweeps	79
Total Azimuth Angle Coverage	$0^\circ - 360^\circ$
Azimuth Increment Rate	0.05°
Total Aspect Angle for Each File	3.9
Total Elevation Angle Coverage	$29.3^\circ - 30.7^\circ$
Elevation Incremental Rate	0.14°
Resolution (Range \times Cross-Range)	1 foot \times 1 foot
Effective Baseline Coverage	0.15m - 4.23m

condition (as depicted in Fig. 2), the height (H_{3A}) estimation can be performed through the following equations [6], [28].

$$H_{3A} = \frac{c}{4\pi f_0} R_0 \left(\frac{\Delta\theta_V}{d_v} \cos \phi - \frac{\Delta\theta_H}{d_H} \sin \phi \right) \quad (15)$$

TABLE III
COMPARISON OF SINGLE-POLARIMETRY (SINGLE-POL) INISAR AND FULL-POLARIMETRY (FULL-POL) INISAR RESULTS BASED ON THE BOAT SIMULATOR DATA

Noise Condition	Mean Coherence (Single-pol InISAR)	Mean Coherence (Full-pol InISAR)
Without Noise	0.9265	0.9393
With Noise (SNR 40 dB)	0.9261	0.9367
With Noise (SNR 30 dB)	0.8963	0.9329

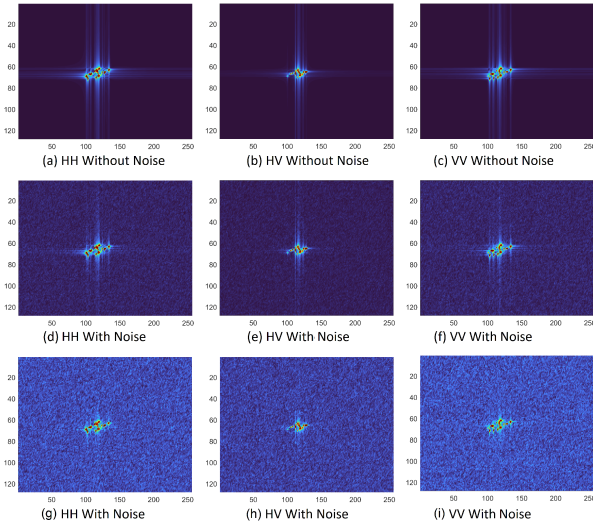


Fig. 6. HH, HV, and VH channel ISAR images before and after adding noise. (a)–(c) Without noise (d)–(f) With noise (SNR 40 dB) (g)–(i) With noise (SNR 30 dB).

$$V_C = \frac{R_0 \Omega}{2\pi} \left(\frac{\Delta\theta_H}{d_H} \cos\phi + \frac{\Delta\theta_V}{d_V} \sin\phi \right) \quad (16)$$

where c is the speed of light, f_0 , d_H , and d_V are the radar-geometry parameters indicating central frequency, horizontal baseline, and vertical baseline. The angles $\Delta\theta_V$ and $\Delta\theta_H$ are the interferometry angles between antennas: V_ξ & C_ξ , and H_ξ & C_ξ , respectively. The angle ϕ in (15) is the angle between y_3 and Ω_{eff} , as shown in Fig. 2. As suggested in [6], [28], the ϕ angle and Ω indicating orientation and modulus of Ω_{eff} , can be calculated through (16), by means of the least square error approach.

III. DATASET DESCRIPTION

Validation of the proposed Pol-InISAR based method is carried out by using simulated as well as a real polarimetric ISAR datasets. The implemented simulated polarimetric ISAR data is a combination of point-like scatterers forming a boat type structure. Furthermore, the implemented real polarimetric ISAR data of a full-size Tank-72 (T72) is captured under Moving and Stationary Target Acquisition and Recognition (MSTAR) program by Georgia Technology Research Institute (GTRI). The Radar Geometry and the complete description of both the used datasets are added in the subsections below.

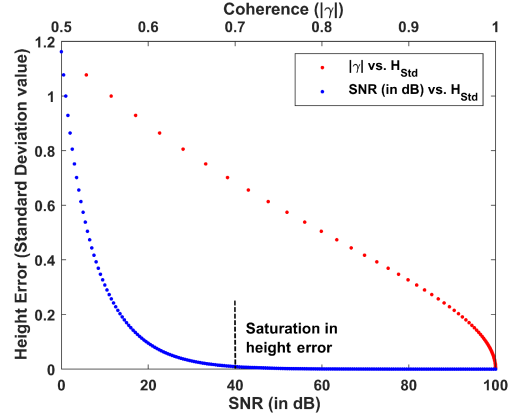


Fig. 7. The plot of height error (standard deviation value) in meter versus coherence ($|\gamma|$) and signal to noise ratio (SNR in dB).

A. Radar Geometry and Dataset Description of Simulated Boat Data

The radar geometry of the simulator is shown in Fig. 2. The assumed geometry is the conventional 3D InISAR imaging geometry that contains three antennas located in the same plane orthogonal to the line of sight (LOS) and simultaneously lying on two orthogonal baselines as depicted in Fig. 2. The concept is to utilize three 2D complex ISAR images obtained from the three antennas V_ξ , C_ξ , and H_ξ , possessing similar range- and cross-range patterns but different phases [11]. Further, the processing of the phase information can lead to the three-dimensional position of the scatterers (through (15) and (16)). R_0 in Fig. 2 indicates the radar-target distance and is aligned with ξ_2 . Ω_T is the angular rotation vector which is applied to the center O of the target. The projection of Ω_T onto the plane orthogonal to the LOS defines the effective rotation vector Ω_{eff} . The IPP is the plane orthogonal to Ω_{eff} . In this in-house developed boat simulator, we use 24 scatterer points situated in such a way that they resemble a boat like structure (an old military minesweeper ship named “Astice”) as depicted in Fig. 3. The advantage of using a simulated point-like target is that it allows point-to-point comparison between the actual target model and the reconstructed one and therefore to numerically evaluate the accuracy of the reconstruction, as performed in the Section IV. The real image of the target, and the corresponding CAD model are shown in Fig. 3(a) and (b), respectively, whereas, the implemented scatterer points-like boat simulator is shown in 3(c). The real boat is capable of generating six following different types of scattering mechanisms [30], [31].

$$\begin{aligned} [S]_s &= \begin{bmatrix} 1 & 0 \\ 0 & 1 \end{bmatrix}; [S]_{bi} = \begin{bmatrix} 1 & 0 \\ 0 & -1 \end{bmatrix}; [S]_{odi} = \begin{bmatrix} \cos 2\tau & \sin 2\tau \\ \sin 2\tau & -\cos 2\tau \end{bmatrix}; \\ [S]_M &= \begin{bmatrix} 0 & 1 \\ 1 & 0 \end{bmatrix}; [S]_{od} = \begin{bmatrix} \cos^2 \tau & \frac{1}{2} \sin 2\tau \\ \frac{1}{2} \sin 2\tau & \sin^2 \tau \end{bmatrix}; [S]_H = \begin{bmatrix} 1 & \pm j \\ \pm j & -1 \end{bmatrix} \end{aligned} \quad (17)$$

where τ indicates orientation angle of scattering structure. To make the target constituting more realistic scatterers, the scattering matrix of each 24 scatterers are randomly selected within

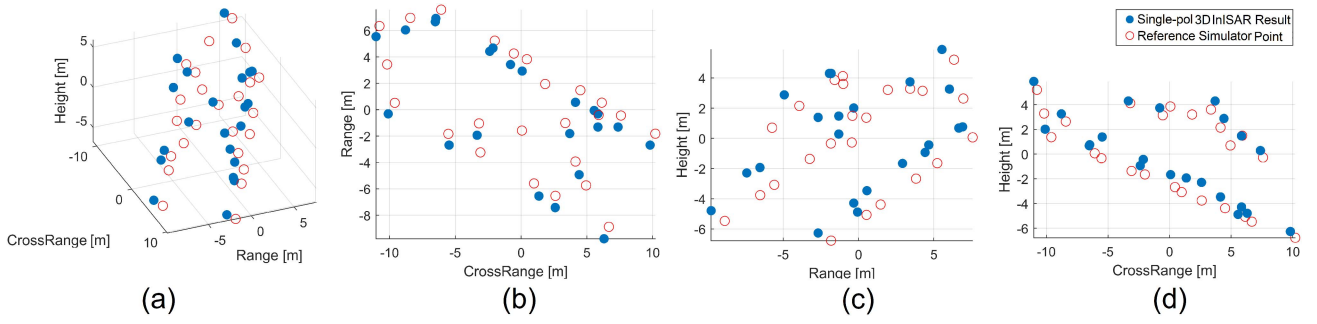


Fig. 8. Three dimensional single-polarimetry (single-pol) InSAR results of boat simulator for without-noise condition (a) 3D view (b) XY-plane view (c) YZ-plane view (d) XZ-plane view. The error parameters obtained for this condition are $MDE = 1.9613$ and $RMSE = 1.5690$.

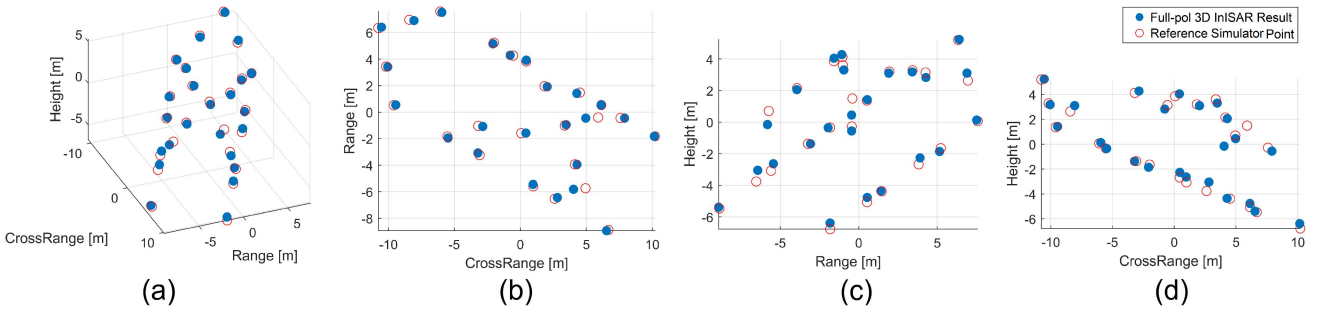


Fig. 9. Three dimensional full-polarimetry (full-pol) InSAR results of boat simulator for without-noise condition (a) 3D view (b) XY-plane view (c) YZ-plane view (d) XZ-plane view. The error parameters obtained for this condition are $MDE = 0.4004$ and $RMSE = 0.2946$.

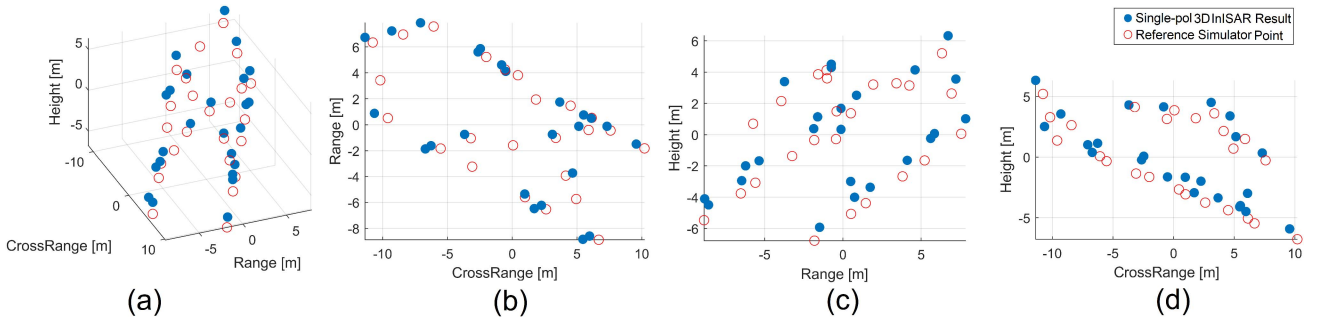


Fig. 10. Three Dimensional single-polarimetry (single-pol) InSAR results of boat simulator for with-noise $SNR = 40$ dB condition (a) 3D view (b) XY-plane view (c) YZ-plane view (d) XZ-plane view. The error parameters obtained for this condition are $MDE = 2.1962$ and $RMSE = 1.9076$.

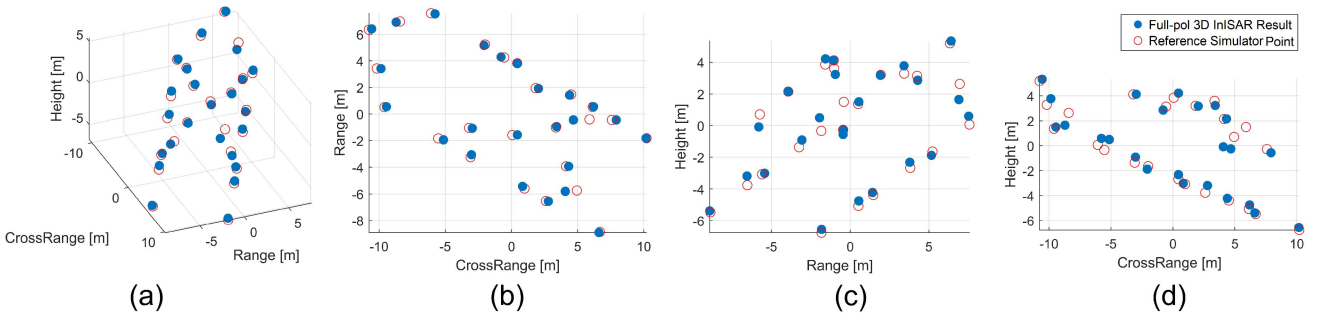


Fig. 11. Three dimensional full-polarimetry (full-pol) InSAR results of boat simulator for with-noise $SNR = 40$ dB condition (a) 3D view (b) XY-plane view (c) YZ-plane view (d) XZ-plane view. The error parameters obtained for this condition are $MDE = 0.5027$ and $RMSE = 0.3840$.

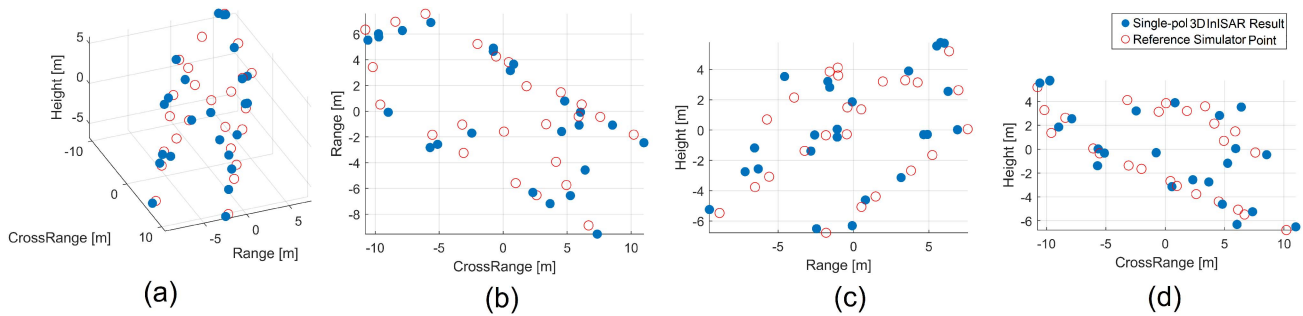


Fig. 12. Three Dimensional single-polarimetry (single-pol) InSAR results of boat simulator for with-noise SNR = 30 dB condition (a) 3D view (b) XY-plane view (c) YZ-plane view (d) XZ-plane view. The error parameters obtained for this condition are MDE = 2.9815; RMSE = 2.7236.

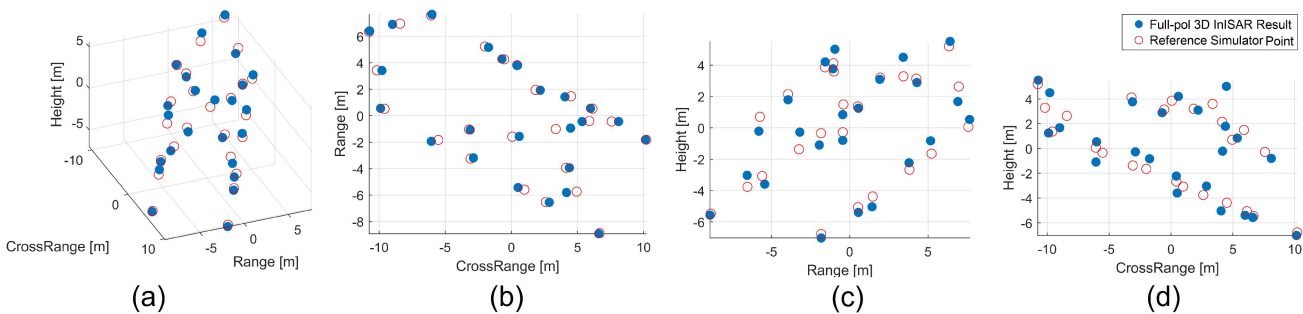


Fig. 13. Three dimensional full-polarimetry (full-pol) InSAR results of boat simulator for with-noise SNR 30 dB condition (a) 3D view (b) XY-plane view (c) YZ-plane view (d) XZ-plane view. The error parameters obtained for this condition are MDE = 0.6930 and RMSE = 0.4607.

TABLE IV
COMPARISON OF SINGLE-POLARIMETRY (SINGLE-POL) INISAR AND FULL-POLARIMETRY (FULL-POL) INISAR RESULTS BASED ON REAL TANK-72 DATA

Elevation-Azimuth Angle Pair		Mean Coherence (Single-pol InSAR)	Mean Coherence (Full-pol InSAR)
Elevation Angle pair	Azimuth Angle		
$[\theta_{el}, \theta_{el} + \Delta\theta_{el}]$	(θ_{az})		
$[29.5754^\circ, 29.7162^\circ]$	48.7250°	0.9132	0.9454
$[29.7162^\circ, 29.8603^\circ]$	48.7250°	0.9115	0.9484
$[29.8603^\circ, 29.9994^\circ]$	48.7250°	0.9339	0.9752
$[29.9994^\circ, 30.1409^\circ]$	48.7250°	0.9233	0.9455
$[30.1409^\circ, 30.2801^\circ]$	48.7250°	0.9196	0.9627
$[29.5754^\circ, 29.7162^\circ]$	91.2250°	0.9316	0.9755
$[29.7162^\circ, 29.8603^\circ]$	91.2250°	0.9265	0.9752
$[29.8603^\circ, 29.9994^\circ]$	91.2250°	0.9228	0.9731
$[29.9994^\circ, 30.1409^\circ]$	91.2250°	0.9166	0.9730
$[30.1409^\circ, 30.2801^\circ]$	91.2250°	0.9234	0.9742
$[29.5754^\circ, 29.7162^\circ]$	133.7250°	0.9224	0.9781
$[29.7162^\circ, 29.8603^\circ]$	133.7250°	0.9174	0.9677
$[29.8603^\circ, 29.9994^\circ]$	133.7250°	0.9206	0.9317
$[29.9994^\circ, 30.1409^\circ]$	133.7250°	0.9038	0.9441
$[30.1409^\circ, 30.2801^\circ]$	133.7250°	0.9179	0.9621

TABLE V
THE ACTUAL AND RECONSTRUCTED SHAPE DIMENSIONS OF TANK-72

Tank \ Dimension	L	W	H	$\frac{L}{W}$	$\frac{L}{H}$	$\frac{W}{H}$	Ext. Gun
Actual Tank-72	9.54	3.59	2.23	2.66	4.28	1.61	2.58
Full-pol 3D InSAR	11.22	4.20	2.57	2.67	4.36	1.63	2.41
Single-pol 3D InSAR	11.00	6.52	6.62	1.68	1.66	0.99	1.72

the aforementioned six scattering mechanisms. Among these six scattering mechanism types, the surface (S), dihedral (Di), and oriented-dihedral (ODi) type scattering generation are prevalent which occur due to boat-deck, boat-dihedrals, or boat-sea-dihedral. The part of antenna, tower, and guardrails of boat are made up of dipole like structures and hence can contribute to H, V, or oriented dipole scattering mechanisms. The four dipoles in combination can generate helix scattering mechanism too [31], [32]. Also, the complex structures on the boat can contribute in multiple-bounces generating multiple-interaction or volume scattering mechanism [31]. The complete list of the parameters, used to simulate the corresponding boat simulator data is added in Table I.

B. Radar Geometry and Dataset Description of Real Tank-72 Data

The target Tank-72 is a Soviet-designed main battle tank of dimension 9.54 m (length) \times 3.59 m (width) \times 2.23 m (height) [33]. The actual image of Tank-72 is shown in Fig. 4. The real Tank-72 ISAR data was collected by performing turntable experiment similar to the one depicted in Fig. 5. The parameters θ_{az} , θ_{el} , and R_0 , mentioned in Fig. 5 indicate nominal azimuth angle, elevation angle, and radar-target distance, respectively. The complete dataset is publicly available and can be accessed through Air Force Research Laboratory (AFRL) website [34]. The whole data is stored in 29 different folders each one corresponding to a specific elevation angle. Each folder contains 85 fully-polarimetric files, corresponding to the 85 different

θ_{az} . Each file contains the target echo recorded from 79 angles equally spaced of approximately 0.05° forming 3.90° around the nominal azimuth angle of θ_{az} . Data have been acquired using a central frequency equals to 9.6 GHz. The 221 frequency samples equally spaced by 3 MHz covering a total bandwidth of 660 MHz are collected. The range and cross-range resolution of this data is $1 \text{ ft} \times 1 \text{ ft}$. In this paper, 6 different elevation angle based T72 ISAR datasets are used that forms 5 elevation angle pairs ($[\theta_{el}, \theta_{el} + \Delta\theta_{el}]$) generating five interferograms for a fixed nominal azimuth angle. Further, three different azimuth angles (as depicted in Fig. 5) have been selected that forms combinedly 15 interferogram pairs. The detailed list of the radar parameters associated with this Tank-72 data is summarized in Table II.

IV. RESULTS AND ANALYSIS

The results and the corresponding analysis of the proposed Pol-InSAR based 3D imaging are reported in the subsequent subsections. For both the implemented datasets (simulated and real), the results are compared with single-polarimetry InSAR 3D imaging methods.

A. Validation of the Proposed 3D Pol-InSAR Imaging by Using Simulated Boat Data

The coherence values obtained by using single-pol InSAR and full-pol InSAR boat simulator data are calculated and reported in Table III for comparison. For full-pol condition, the coherence values are evaluated with the help of (11)–(13) whereas, for the single-pol condition, the coherence values are evaluated as $\sum_{i=1}^3 \sum_{j=1 \neq i}^3 |\gamma_{ij}^{\text{HH}}|$, where

$$\gamma_{ij}^{\text{HH}} = \frac{\langle S_{\text{HH}}^i S_{\text{HH}}^{j*} \rangle}{\sqrt{\langle S_{\text{HH}}^i S_{\text{HH}}^{i*} \rangle \langle S_{\text{HH}}^j S_{\text{HH}}^{j*} \rangle}} \quad (18)$$

Further, the mean coherence is evaluated by averaging the coherence values of all the scatterers taken under consideration for 3D point cloud formation. The coherence results are generated for with- and without-noise scenarios to make the performance analysis more robust. In with-noise condition, the white Gaussian noise are added directly to the data in the ISAR image domain. The two different with-noise conditions of $\text{SNR} \simeq 40 \text{ dB}$ and $\text{SNR} \simeq 30 \text{ dB}$ are reported in this paper. The SNR is evaluated in the ISAR image and represents the mean signal to noise power ratio in each resolution cell. With- and without-noise ISAR images of all the three polarimetric channels HH, HV, and VV, are shown in Fig. 6(a)–(i) for visual interpretation.

The plot shown in Fig. 7 indicates the standard deviation of the error on the estimated height (H_{Std}) against the SNR and coherence value ($|\gamma|$). The corresponding relationship (shown in (19)) is established with the help of Cramer-Rao bound expression presented in [35], [36].

$$H_{\text{Std}} = \frac{cR_0}{4\pi f_0 d} \times \frac{1}{|\gamma|} \sqrt{\frac{1 - |\gamma|^2}{2L}} \quad (19)$$

where d is the baseline-distance, L is the number of looks, and γ can be expressed in terms of SNR [35], as

$$\gamma = \frac{1}{1 + \frac{1}{\text{SNR}}} \quad (20)$$

By analyzing SNR versus H_{Std} plot, $\text{SNR} = 40 \text{ dB}$ can be considered as the saturation value of the curve. Further, by analyzing coherence versus H_{Std} plot in the same figure, it is worth to observe that the minimum value of H_{Std} can be achieved at the highest possible coherence value. By comparing the results shown in Table III, it is worth to note the improvement in the mean coherence value using full-polarimetry data in comparison with the single-polarimetry. In without-noise or ideal signal receiving condition, the improvement is not extensive while for the noisy scenario, and especially for SNR 30 dB, a significant improvement in the coherence level can be observed. The 3D results generated for both the without- and with-noise scenarios are shown in Figs. 8–13. The images shown in Figs. 8(a)–(d), 10(a)–(d) and 12(a)–(d) indicate the single-pol 3D InSAR based results superimposing with the original reference model points, whereas, Figs. 9(a)–(d), 11(a)–(d), and 13(a)–(d) indicate the full-pol 3D InSAR based results superimposing with the original reference model points, for the conditions of without-noise, with-noise (SNR 40 dB), and with-noise (SNR 30 dB), respectively. In all of these images, the reconstructed 3D points are indicated by the blue filled circles, and the actual reference simulator points are indicated by the red hollow circles. By comparing these images one can conclude that the obtained reconstructed 3D points of full-pol InSAR results are closer to the actual reference simulator points. Contrary to this, in the single-pol InSAR based 3D results, the reconstructed points are missing the actual model (reference) points, indicating poor 3D results generation of the target. Hence, through the visual interpretation, it can be concluded that the proposed approach of full-pol 3D InSAR performs better than the single-pol 3D InSAR. However, for the quantitative performance evaluation, we estimated two parameters: mean distance error (MDE) and Root Mean Square Error (RMSE). MDE results in overall displacement of reconstructed points in comparison with the reference simulator. The formula used to calculate MDE for m number of extracted scatterers, is as follows.

$$\text{MDE} = \sum_{t=1}^m \frac{\sqrt{(R_x^t - M_x^t)^2 + (R_y^t - M_y^t)^2 + (R_z^t - M_z^t)^2}}{m}, \quad (21)$$

where (R_x^t, R_y^t, R_z^t) and (M_x^t, M_y^t, M_z^t) are the t^{th} point's (x, y, z) coordinate of reconstructed results and reference model, respectively. Another standard error evaluation parameter, i.e. RMSE is calculated through (22) to further quantify the mismatch between the reconstructed and original (reference) 3D point cloud.

$$\text{RMSE} = \sqrt{\text{mean}(\|\mathbf{R} - \mathbf{M}\|_F^2)}, \quad (22)$$

where $\|\cdot\|_F$ is Frobenius norm and, \mathbf{R} and \mathbf{M} are the two matrices of dimension $3 \times t$, and each row of \mathbf{R} and \mathbf{M} indicate the t^{th} point's (x, y, z) coordinate of reconstructed results and

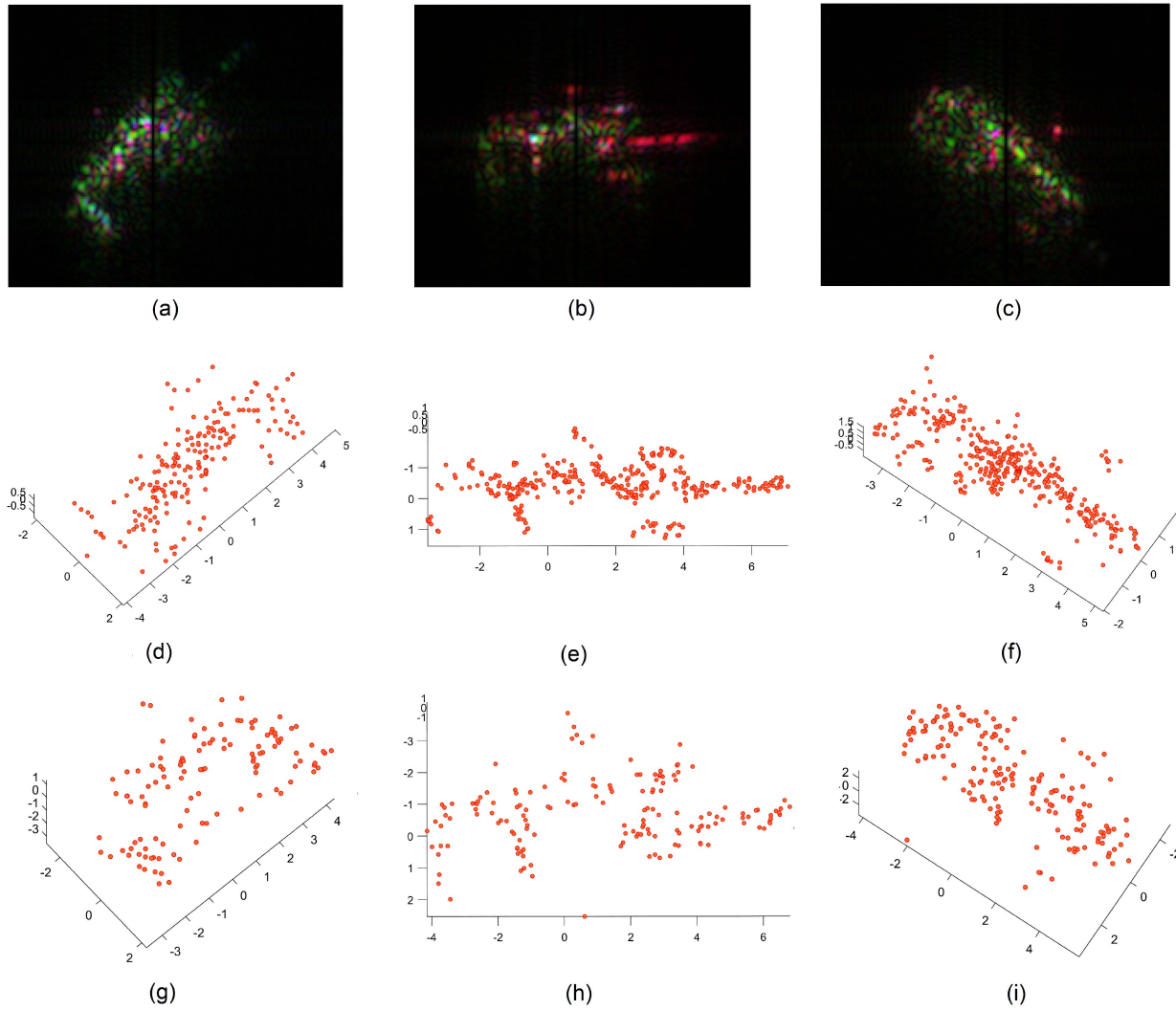


Fig. 14. The results obtained using real Tank-72 data, where (a), (b), & (c) indicate Pauli decomposition false RGB images for azimuth conditions 48.725° , 91.225° , and 133.725° , respectively. (d), (e), & (f) indicate the full-polarimetry (full-pol) InISAR based 3D imaging results for azimuth conditions 48.725° , 91.225° , and 133.725° , respectively. (g), (h), & (i) indicate the single-polarimetry (single-pol) InISAR based 3D imaging results for azimuth conditions 48.725° , 91.225° , and 133.725° , respectively.

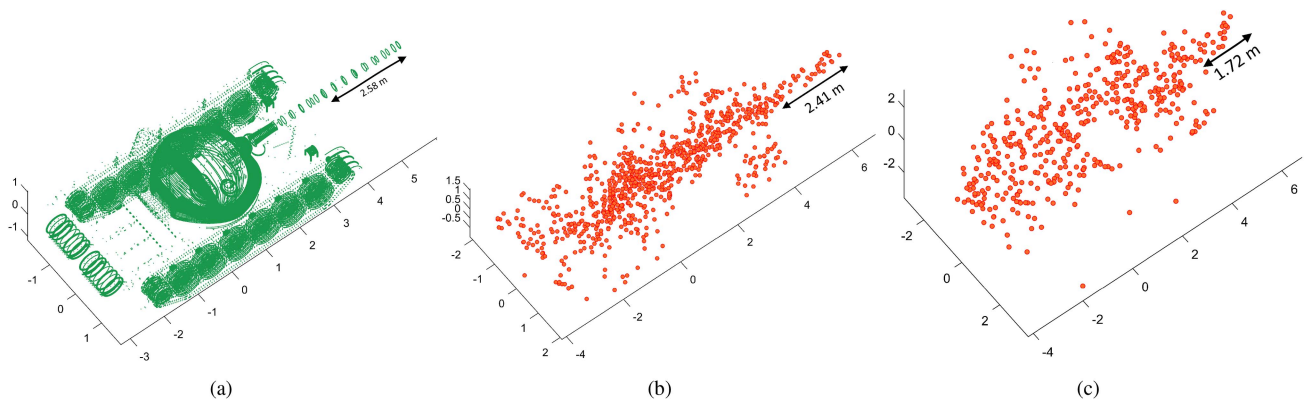


Fig. 15. (a) Tank-72 CAD Model (down-sampled point-cloud) (b) Full-polarimetry (full-pol) InISAR based 3D result (c) Single-polarimetry (single-pol) InISAR based 3D result.

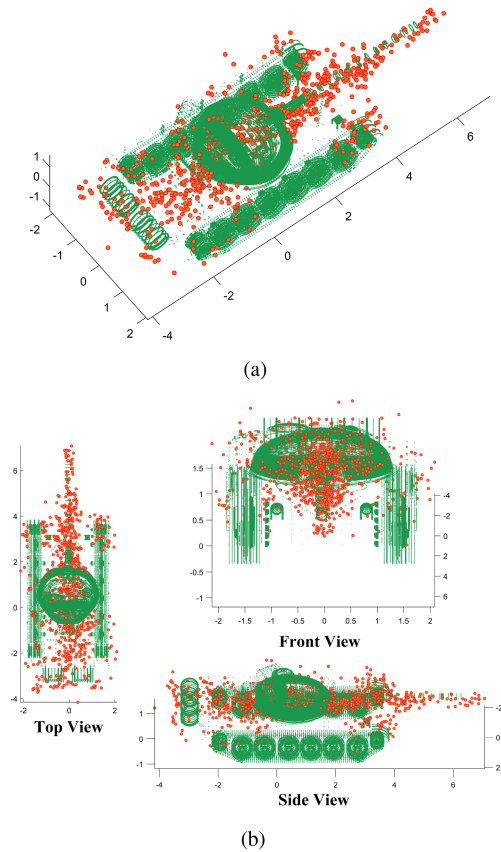


Fig. 16. Superimposition of the results obtained using Full-pol 3D InSAR over target (Tank-72) CAD model. (a) 3D view (b) Top, front, and side views.

reference model, respectively. The MDE and RMSE calculated for the condition of full-pol 3D InSAR and single-pol 3D InSAR, are directly added in the figures to have a clear visibility in comparing the results. The MDE calculated for the condition of full-pol 3D InSAR is 0.4004, 0.5027, and 0.6930 for without-noise, with-noise SNR 40 dB, and with-noise SNR 30 dB conditions, respectively, which indicates better performance over single-pol 3D InSAR that obtains MDE value 1.9613, 2.1962, and 2.9815 for without-noise and SNR 40 dB, and with-noise SNR 30 dB conditions, respectively. Further, the lower RMSE values of 0.2946, 0.3840, and 0.4607 are achieved by using full-pol 3D InSAR in comparison with the RMSE values of 1.5690, 1.9076, and 2.7236 obtained by using single-pol 3D InSAR, for the condition of without-noise, with-noise SNR 40 dB, and with-noise SNR 30 dB, respectively. Hence, with the RMSE parameter also, one can conclude that the full-pol InSAR performs better than the single-pol InSAR.

B. Validation of the Proposed 3D Pol-InSAR Imaging by Using Real Tank-72 Data

The coherence values obtained by using single-pol (HH) and full-pol Tank-72 ISAR data for all the 15 interferogram combinations, based on different azimuth and elevation angles (as described in Section III-B), are added in Table IV. Herein, the full-pol based coherence is evaluated using (4) as explained

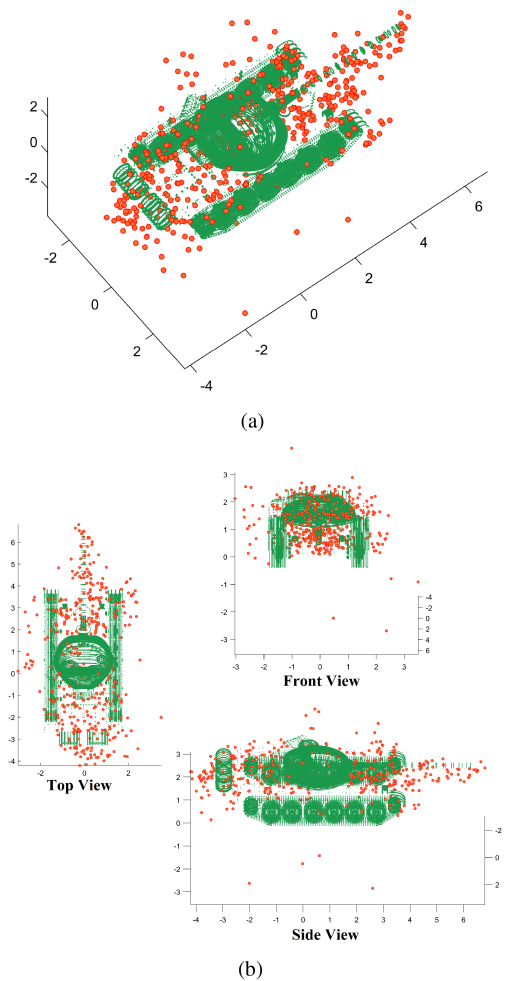


Fig. 17. Superimposition of the results obtained using Single-pol 3D InSAR over target (Tank-72) CAD model. (a) 3D view (b) Top, front, and side views.

in Section II-A and the single-pol coherence is evaluated using (18) by considering $i = 1$ and $j = 2$. By comparing the results, it is possible to note that the coherence value is significantly improved by using the proposed full-pol InSAR method in comparison with the single-pol InSAR, in all the combinations. Also, the full-polarimetry data make it possible to have response in co- as well as cross-pol channel and through that the Pauli RGB decomposed image can be obtained. For, 48.725° , 91.225° , and 133.725° azimuth conditions (at $\theta_{el} = 29.5754$), the false RGB decomposed images are shown in Fig. 14(a), (b), and (c), respectively, where red, blue, and green colors indicate the polarimetric channels $\frac{1}{\sqrt{2}}|HH - VV|$, $\frac{1}{\sqrt{2}}|HH + VV|$, and $\sqrt{2}|HV|$, respectively. It is worth to note the existence of all the three colors in the images, that proves the presence of different class of scatterers in the target generating different scattering mechanisms. And to cover-up all various kinds of scatterers, it is important to utilize the complete polarimetric information inherent in full-pol ISAR data, instead of single-pol ISAR data. Further, different parts of the Tank can be apparently seen in different azimuth angle conditions of 48.725° , 91.225° , and 133.725° , respectively. Therefore, to better detect the Tank in

its full shape, it is important to combine all the azimuth aspects together.

The 3D reconstructed point clouds corresponding to the Tank-72 target, are shown in Fig. 14(d)–(f) and (g)–(i), generated by using full-pol and single-pol InISAR based conditions, respectively, and further, the combined results are shown in Fig. 15(b) and (c) for full-pol and single-pol conditions, respectively. The CAD model of Tank-72 is shown in Fig. 15(a) for reference. By comparing these images, it is possible to observe that the fully-polarimetric results better represent the target shape in comparison with the single-polarimetric results. Further, to numerically measure the performance, the shape of the reconstructed point clouds is compared with the actual shape of the target Tank-72, in terms of its length (L), width (W), and height (H), and the ratios among the three sizes, as shown in Table V.

By observing Table V, it is possible to note that the shape of the target through the dimension ratios: L/H, H/W, and W/H, is preserved in the case of full-pol 3D InISAR reconstructed results, whereas, in case of single-pol 3D InISAR, the width and height are almost equal that differs from the actual Tank-72 shape condition. Another important attribute that separates tank from other vehicles is the Tank-Gun. The length of the Gun part ahead of the tank hull (length 6.95 m), is 2.58 m. The Gun length measured from the 3D reconstructions is reported in Fig. 15(a)–(c) for comparison. The results again validate the better reconstruction by using proposed full-pol InISAR in comparison with single-pol InISAR.

The 3D point cloud, generated by using full-pol and single-pol InISAR methods, as shown in Fig. 15(b) and (c), respectively, are superimposed on the Tank-72 CAD model, and the respective superimposed results are shown in Figs. 16 and 17. Better alignment of point cloud with the CAD model can be seen for the full-pol InISAR based results in comparison with single-pol. Further comparing these results with the ground reference parts of Tank-72, exhibiting main features of the tank (as shown in Fig. 4), it is worth observing that the turret, tank gun, and oil barrel are strongly reconstructed with a large number of scatterer points, whereas the mudguard has moderate and road wheel has a smaller number of reconstructed scatterer points in case of full-pol 3D InISAR result. Conversely, in single-pol 3D InISAR results, these all five key features are not easily visible.

V. CONCLUSION

A new approach of Polarimetric Interferometry Synthetic Aperture Radar (Pol-InISAR) is presented in this paper for the 3D imaging of non-cooperative targets. The use of full-polarimetry data facilitates to obtain interferogram from the all possible polarimetric combinations. By using the coherent optimization approach, the polarimetric channel associated with the highest coherence is selected to generate 3D point cloud. Further, simulated and real data have been used to validate the proposed Pol-InISAR approach. The obtained results have shown that the proposed Pol-InISAR based method performs better than the single-pol based 3D InISAR imaging approach. Improvements have been evaluated by visually comparing the results and using numerical performance indexes. The proposed

Pol-InISAR method is outlined based on the single- and dual-baseline conditions, which can be further extended in future for multi-baseline configuration utilizing N ($\forall N > 3$) number of independent observations together to get more accurate 3D result. The 3D Pol-InISAR results can be further used to recognize the detected target and future research will go in that direction. The work presented in this paper can have a strong impact in military and civil applications where the recognition of targets is of primary importance.

APPENDIX A

The projection vector (w) leading to the highest possible coherence value can be obtained by setting the gradient of $|\gamma_w|^2$ to zero and solving it. For simplicity, we express $|\gamma_w|^2$ of (4) as

$$\gamma_w \gamma_w^* = |\gamma_w|^2 = \frac{aa^*}{bc} \quad (23)$$

where, $a = (w^\dagger \Omega_{12} w)$, $b = (w^\dagger T_{11} w)$, and $c = (w^\dagger T_{22} w)$. The partial derivation of these parameters can be expressed as

$$\begin{aligned} \frac{\partial aa^*}{\partial w^\dagger} &= 2(\Omega_{12} w)(w^\dagger \Omega_{12}^\dagger w) + 2(\Omega_{12}^\dagger w)(w^\dagger \Omega_{12} w), \\ \frac{\partial b}{\partial w^\dagger} &= 2T_{11} w \quad \text{and} \quad \frac{\partial c}{\partial w^\dagger} = 2T_{22} w \end{aligned} \quad (24)$$

The necessary condition of $|\gamma_w|^2 \rightarrow \text{maximum}$ can be achieved if $\nabla |\gamma_w|^2 \rightarrow 0$ and this condition can be expressed with the help of (23) as

$$\frac{\partial(aa^*)}{\partial w^\dagger} bc - aa^* \left(\frac{\partial b}{\partial w^\dagger} c + \frac{\partial c}{\partial w^\dagger} b \right) = 0 \quad (25)$$

By putting the partial derivative terms from (24) along with the a , b , and c values, (25) becomes

$$(a^* \Omega_{12} + a \Omega_{12}^\dagger) w = c |\gamma_w|^2 T_{11} w + b |\gamma_w|^2 T_{22} w \quad (26)$$

This expression converges to the eigenvalue problem by taking into account that the polarimetric information acquired from the two antennas are very closer and captured under small temporal and spatial separations that leads to the similarities in the second-order statistical matrices, i.e. $a \approx a^* \approx b \approx c$ [22], [24], [37]. Considering this condition, (26) converges to the following eigenvalue problem [22], [38]:

$$(T_{11} + T_{22})^{-1} (\Omega_{12} + \Omega_{12}^\dagger) w = |\gamma_w|^2 w \quad (27)$$

Equation (27) yields three eigenvalues. The highest among these three eigenvalues corresponds to the optimum coherence value and the eigenvector corresponding to this maximum eigenvalue results in the desired projection vector.

REFERENCES

- [1] W. G. Carrara, R. S. Goodman, and R. M. Majewski, *Spotlight Synthetic Aperture Radar: Signal Processing Algorithms*. Norwood, MA, USA: Artech House, 1995.
- [2] V. C. Chen and M. Martorella, *Inverse Synthetic Aperture Radar Imaging: Principles, Algorithms and Applications*. New York, NY, USA: Inst. Eng. Technol., 2014.
- [3] D. A. Ausherman, A. Kozma, J. L. Walker, H. M. Jones, and E. C. Poggio, "Developments in radar imaging," *IEEE Trans. Aerosp. Electron. Syst.*, vol. AES-20, no. 4, pp. 363–400, Jul. 1984.

- [4] P. Huang et al., "High-resolution ISAR imaging for maneuvering targets based on iterative adaptive processing," *IEEE Trans. Comput. Imag.*, vol. 7, pp. 1093–1108, 2021.
- [5] M. Martorella, Ed., *Multidimensional Radar Imaging* (Radar, Sonar & Navigation Series). Stevenage, U.K.: Inst. Eng. Technol., 2019. [Online]. Available: <https://digital-library.theiet.org/content/books/ra/sbra527e>
- [6] M. Martorella, D. Stagliano, F. Salvetti, and N. Battisti, "3D interferometric ISAR imaging of noncooperative targets," *IEEE Trans. Aerosp. Electron. Syst.*, vol. 50, no. 4, pp. 3102–3114, Oct. 2014.
- [7] Z. Jiao, C. Ding, L. Chen, and F. Zhang, "Three-dimensional imaging method for array ISAR based on sparse Bayesian inference," *Sensors*, vol. 18, no. 10, 2018, Art. no. 3563.
- [8] M. Iwamoto and T. Kirimoto, "A novel algorithm for reconstructing three-dimensional target shapes using sequential radar images," in *Proc. IEEE Int. Geosci. Remote Sens. Symp.*, 2001, pp. 1607–1609.
- [9] X. Xu and R. M. Narayanan, "Three-dimensional interferometric ISAR imaging for target scattering diagnosis and modeling," *IEEE Trans. Image Process.*, vol. 10, no. 7, pp. 1094–1102, Jul. 2001.
- [10] J. A. Given and W. R. Schmidt, "Generalized ISAR-Part II: Interferometric techniques for three-dimensional location of scatterers," *IEEE Trans. Image Process.*, vol. 14, no. 11, pp. 1792–1797, Nov. 2005.
- [11] G. Wang, X.-G. Xia, and V. C. Chen, "Three-dimensional ISAR imaging of maneuvering targets using three receivers," *IEEE Trans. Image Process.*, vol. 10, no. 3, pp. 436–447, Mar. 2001.
- [12] K. Wu and X. Xu, "A fast ISAR tomography technique for fully polarimetric 3-D imaging of man-made targets," *IEEE Trans. Geosci. Remote Sens.*, vol. 60, pp. 1–12, 2022.
- [13] J. Zhang and Y. Wang, "A three-dimensional imaging method of ship target via multistatic distributed InISAR," *IEEE Geosci. Remote Sens. Lett.*, vol. 19, pp. 1–5, 2022.
- [14] M. Martorella, F. Salvetti, D. Stagliano, and E. Giusti, "Three-dimensional ISAR imaging: A review," *IET J. Eng.*, vol. 2019, pp. 6823–6828, Oct. 2019.
- [15] F. Salvetti, M. Martorella, E. Giusti, and D. Stagliano, "Multiview three-dimensional interferometric inverse synthetic aperture radar," *IEEE Trans. Aerosp. Electron. Syst.*, vol. 55, no. 2, pp. 718–733, Apr. 2019.
- [16] A. Fontana, P. Berens, D. Stagliano, and M. Martorella, "3D InISAR target reconstruction using airborne PAMIR data," in *Proc. IEEE 11th Eur. Conf. Synthetic Aperture Radar*, 2016, pp. 1–5.
- [17] A. Fontana, P. Berens, D. Stagliano, and M. Martorella, "3D ISAR/SAR imaging using multichannel real data," in *Proc. IEEE Radar Conf.*, 2016, pp. 1–4.
- [18] C.-A. Deledalle, L. Denis, and F. Tupin, "NL-InSAR: Nonlocal interferogram estimation," *IEEE Trans. Geosci. Remote Sens.*, vol. 49, no. 4, pp. 1441–1452, Apr. 2011.
- [19] S. R. Cloude and K. P. Papathanassiou, "Polarimetric SAR interferometry," *IEEE Trans. Geosci. Remote Sens.*, vol. 36, no. 5, pp. 1551–1565, Sep. 1998.
- [20] J. L. Gomez-Dans, "On the use of polarimetry and interferometry for SAR image analysis," Ph.D. dissertation, Sheffield Centre Earth Obs. Sci., Univ. Sheffield, Sheffield, U.K., 2004.
- [21] J. L. Gomez-Dans and S. Quegan, "Constraining coherence optimization in polarimetric interferometry of layered targets," in *Proc. POLInSAR*, 2005, pp. 1–6.
- [22] E. Colin, C. Titin-Schnaider, and W. Tabbara, "Investigation on Different Interferometric Coherence Optimization Methods," in *Proc. Appl. SAR Polarimetry Polarimetric Interferometry* (ESA Special Publication Series), H. Lacoste, Ed., 2003, Art. no. 74.1.
- [23] E. Colin, C. Titin-Schnaider, and W. Tabbara, "An interferometric coherence optimization method in radar polarimetry for high-resolution imagery," *IEEE Trans. Geosci. Remote Sens.*, vol. 44, no. 1, pp. 167–175, Jan. 2006.
- [24] M. Neumann, L. Ferro-Famil, and A. Reigber, "Multibaseline polarimetric SAR interferometry coherence optimization," *IEEE Geosci. Remote Sens. Lett.*, vol. 5, no. 1, pp. 93–97, Jan. 2008.
- [25] F. Mancuso, E. Giusti, A. Kumar, S. Ghio, and M. Martorella, "Comparative assessment of polarimetric features estimation in fully polarimetric 3D-ISAR imaging system," in *Proc. IET Int. Radar Conf.*, 2022, pp. 353–358.
- [26] M. Martorella, A. Cacciamano, E. Giusti, F. Berizzi, B. Haywood, and B. Bates, "CLEAN technique for polarimetric ISAR," *Int. J. Navigation Observ.*, vol. 2008, pp. 1–13, Aug. 2008.
- [27] B. Tian, Z. Lu, Y. Liu, and X. Li, "Review on interferometric ISAR 3D imaging: Concept, technology and experiment," *Signal Process.*, vol. 153, pp. 164–187, 2018.
- [28] E. Giusti, S. Ghio, and M. Martorella, "Drone-based 3D interferometric ISAR imaging," in *Proc. IEEE Radar Conf.*, 2021, pp. 1–6.
- [29] D. Li and Y. Zhang, "A fast normalized cross-correlation algorithm for InSAR image subpixel registration," in *Proc. IEEE 3rd Int. Asia-Pacific Conf. Synthetic Aperture Radar*, 2011, pp. 1–4.
- [30] G. Margarit, J. J. Mallorqui, J. Fortuny-Guasch, and C. Lopez-Martinez, "Phenomenological vessel scattering study based on simulated inverse SAR imagery," *IEEE Trans. Geosci. Remote Sens.*, vol. 47, no. 4, pp. 1212–1223, Apr. 2009.
- [31] Y. Li et al., "Ship recognition from chaff clouds with sophisticated polarimetric decomposition," *Remote Sens.*, vol. 12, no. 11, 2020, Art. no. 1813.
- [32] Y. Yamaguchi, T. Moriyama, M. Ishido, and H. Yamada, "Four-component scattering model for polarimetric SAR image decomposition," *IEEE Trans. Geosci. Remote Sens.*, vol. 43, no. 8, pp. 1699–1706, Aug. 2005.
- [33] "T-72 A MBT Main Battle Tank-Russia," Dec. 2021. Accessed: May 29, 2022. [Online]. Available: <https://www.armyrecognition.com>
- [34] U. A. Force, "Sensor data management system (SDMS)," 1997. Accessed: Dec. 23, 2021. [Online]. Available: <https://www.sdms.af.mil/>
- [35] P. A. Rosen et al., "Synthetic aperture radar interferometry," *Proc. IEEE*, vol. 88, no. 3, pp. 333–382, Mar. 2000.
- [36] F. Rocca, A. Ferretti, A. V. Monti-Guarnieri, C. M. Prati, and D. Massonnet, "InSAR Processing: A Mathematical Approach (part C)," in *InSAR principles: guidelines for SAR interferometry processing and interpretation*, K. Fletcher, Ed., Noordwijk, The Netherlands: ESA Publications, 2007, pp. 1–115.
- [37] E. Colin, C. Titin-Schnaider, and W. Tabbara, "Coherence optimization methods for scattering centers separation in polarimetric interferometry," *J. Electromagn. Waves Appl.*, vol. 19, no. 9, pp. 1237–1250, 2005.
- [38] E. C. Koeniguer, "Polarimetric radar images," Ph.D. dissertation, Signal and image processing, Université Paris Sud, Orsay, France, Nov. 2014.



Ajeet Kumar (Member, IEEE) received the Ph.D. degree in RF and microwave engineering from the ECE Department, Indian Institute Of Technology Roorkee, Roorkee, India, in 2019. From 2014 to 2017, he was a Research Fellow (Junior and Senior) at the Indian Space Research Organization Mission of Radar Imaging Satellites (RISAT-1). Further, as a Postdoc Researcher, he was a Research Associate for one year in another ISRO space-borne mission of Chandrayaan-2. He is currently a full-time Researcher (Researcher Level IV) with the CNIT - National Laboratory of Radar and Surveillance Systems, Italy, and working on the Office of Naval Research Global (ONR Global) sponsored project of ATR by means of Polarimetric ISAR Images and multi-view 3D InISAR. His research interests include polarimetric SAR, hybrid-polarimetry SAR, interferometry SAR, and inverse SAR based radar applications. He is recently elevated to a Senior Grade Member of the International Union of Radio Science for his vital contribution as a Radio Scientist. He was the recipient of the prestigious YSA (Young Scientist Award) given by the side of URSI.



Elisa Giusti (Member, IEEE) received the Telecommunication Engineering Laurea (*cum laude*) and Ph.D. degrees from the University of Pisa, Pisa, Italy, in 2006 and 2010, respectively. From June 2009 to November 2014, she was a Researcher under contract with the Department of Information Engineering, University of Pisa. From November 2014 to December 2015, she was a Researcher under contract at the CNIT-RaSS National Laboratory. Since December 2015, she has been a permanent Researcher with the CNIT-RaSS National Laboratory, Pisa. Since 2009,

she has been involved as a Researcher in several international projects funded by Italian ministries (Ministry of Defence, Ministry of Economic Development) and European organisations (EDA, ESA). She is the Co-founder of a radar systems-related spin-off company, ECHOES radar technologies, Pisa. She is a co-author of more than 80 papers and seven book chapters. She is the Editor of a book titled *Radar Imaging for Maritime Observation*, CRC press. Her main research interests include radar imaging, including active, passive, bistatic, multistatic, and polarimetric radar. She was the recipient of the 2016 Outstanding Information Research Foundation Book publication Award for the book *Radar Imaging for Maritime Observation*, and Fall 2021 SET Panel Early Career Award (SPECA).



Francesco Mancuso (Graduate Student Member, IEEE) received the master's degree (*cum laude*) in telecommunication engineering in 2021 from the University of Pisa, Pisa, Italy, where he is currently working toward the Ph.D. degree with the Department of Information Engineering, and he collaborates with the Radar and Surveillance System National Laboratory, Pisa. His main research interests include radar imaging (ISAR) and radar signal processing.



Alberto Lupidi (Member, IEEE) was born in Livorno, Italy, in December of 1982. He received the M.Sc. degree in telecommunication engineering and the Ph.D. degree in remote sensing from the University of Pisa, Pisa, Italy, in September 2008 and 2013, respectively. During the year 2012, he spent a research period with TU Delft, Delft, The Netherlands, where he focused on the processing of polarimetric weather data and the decomposition of polarimetric data. He is currently a Researcher with the National Laboratory of Radar and Surveillance Systems, CNIT. He was involved in various projects funded by Italian Government agencies (such as the Ministry of Defence and Ministry of Economic Development), and European and international organizations (such as EDA and NATO). His areas of expertise and interest lie in the fields of radar systems, signal and data processing, weather radar polarimetry, SAR polarimetry, machine learning, and quantum radar. His research interests include marine environment sensing, oil spill detection, and monitoring illegal maritime activities.



Selenia Ghio (Member, IEEE) received the bachelor's and master's (with Hons.) degrees in telecommunication engineering and the Ph.D. degree in information engineering with the University of Pisa, Pisa, Italy, in 2012, 2015, and 2019, respectively. She is currently a Researcher with the National Laboratory of Radar and Surveillance Systems, CNIT. Her main research interests include radar signal processing, SSA, objects' feature extraction for identification, time-frequency analysis, deep neural network applications in target classification, and 3D radar imaging.

During her Ph.D., she was hosted for six months with ESA/ESOC, Darmstadt, Germany, for a collaboration with the Space debris team. She was involved in several project funded by Italian ministries (Ministry of Defence and Ministry of Economic Development) and European organizations (EDA). She was the recipient of the Amelia Earhart Fellowship in 2018.



Marco Martorella (Fellow, IEEE) received the Laurea degree (Bachelor+Masters) in telecommunication engineering and the Ph.D. degree in remote sensing from the University of Pisa, Pisa, Italy, in 1999 and 2003, respectively. He is currently a Professor and the Chair with RF and Space Sensing Department, University of Birmingham, Birmingham, U.K. He is also the Vice-Director of the CNIT's National Radar and Surveillance Systems Laboratory. He is the Co-founder of ECHOES, a radar systems-related spin-off company. He is the author of more than 200

international journal and conference papers, three books and 17 book chapters. His main research interests include radar, with specific focus on radar imaging, multichannel radar and space situational awareness. He has presented several tutorials at international radar conferences, has lectured at NATO Lecture Series and organised international journal special issues on radar imaging topics. He is a Member of the IEEE AES RADAR SYSTEMS PANEL, a Member of the NATO SET Panel, where he sits as the Co-Chair of the Radio Frequency Technology Focus Group, and a Member of the EDA Radar Captech. He has chaired several NATO research activities, including three Research Task Groups, one Exploratory Team and two Specialist Meetings. He was the recipient of the 2008 Italy-Australia Award for young researchers, 2010 Best Reviewer for the IEEE GRSL, IEEE 2013 Fred Nathanson Memorial Radar Award, 2016 Outstanding Information Research Foundation Book publication award for the book *Radar Imaging for Maritime Observation*, and 2017 NATO Set Panel Excellence Award.

Open Access funding provided by 'Università di Pisa' within the CRUI CARE Agreement